



SMA Observations of the Hot Molecular Core IRAS 18566+0408

Andrea Silva^{1,2,3} , Qizhou Zhang¹ , Patricio Sanhueza³ , Xing Lu³ , Maria T. Beltrán⁴ , Cassandra Fallscheer⁵,
Henrik Beuther⁶ , T. K. Sridharan¹, and Riccardo Cesaroni⁴

¹ Harvard-Smithsonian Center for Astrophysics, 60 Garden Street, Cambridge, MA 02138, USA; andrea.silva@tufts.edu

² Department of Physics and Astronomy, Tufts University, Medford, MA 02155, USA

³ National Astronomical Observatory of Japan, National Institutes of Natural Sciences, 2-21-1 Osawa, Mitaka, Tokyo 181-8588, Japan

⁴ INAF—Osservatorio Astrofisico di Arcetri, Largo E. Fermi 5, I-50125, Italy

⁵ Central Washington University, 400 E University Way, Ellensburg, WA 98926, USA

⁶ Max-Planck Institute for Astronomy, Königstuhl 17, D-69117 Heidelberg, Germany

Received 2017 May 31; revised 2017 August 21; accepted 2017 August 24; published 2017 September 25

Abstract

We present Submillimeter Array (SMA) observations toward the high-mass star-forming region IRAS 18566+0408. Observations at the 1.3 mm continuum and in several molecular line transitions were performed in the compact ($2''.4$ angular resolution) and very-extended ($\sim 0''.4$ angular resolution) configurations. The continuum emission from the compact configuration shows a dust core of $150 M_{\odot}$, while the very-extended configuration reveals a dense ($2.6 \times 10^7 \text{ cm}^{-3}$) and compact (~ 4000 au) condensation of $8 M_{\odot}$. We detect 31 molecular transitions from 14 species including CO isotopologues, SO, CH₃OH, OCS, and CH₃CN. Using the different k -ladders of the CH₃CN line, we derive a rotational temperature at the location of the continuum peak of 240 K. The ¹²CO(2–1), ¹³CO(2–1), and SO(6₅–5₄) lines reveal a molecular outflow at PA $\sim 135^\circ$ centered at the continuum peak. The extended ¹²CO(2–1) emission has been recovered with the IRAM 30 m telescope observations. Using the combined data set, we derive an outflow mass of $16.8 M_{\odot}$. The chemically rich spectrum and the high rotational temperature confirm that IRAS 18566+0408 is harboring a hot molecular core. We find no clear velocity gradient that could suggest the presence of a rotational disk-like structure, even at the high-resolution observations obtained with the very-extended configuration.

Key words: ISM: individual objects (IRAS 18566+0408) – ISM: jets and outflows – ISM: kinematics and dynamics – stars: formation – stars: massive

1. Introduction

The study of the formation of high-mass stars, especially in the early evolutionary phases, has been observationally challenging due to the large distances involved ($d \geq 1$ kpc), complex cluster environments ($n_{*} \gtrsim 100 \text{ pc}^{-3}$), and short evolutionary timescales ($t_{\text{KH}} \leq 10^4$ years for a O-type star) in comparison with the study of low-mass stars. Early stages of massive star formation have numerous observational signatures, including molecular masers (e.g., Wang et al. 2006; Cyganowski et al. 2012), outflows (e.g., Zhang et al. 2001, 2005; Beuther et al. 2002b; Qiu et al. 2008), chemically evolved regions (e.g., Sanhueza et al. 2012; Wang et al. 2014; Sanchez-Monge et al. 2017), hot molecular cores (HMCs; e.g., Garay & Lizano 1999; Beltrán & de Wit 2016), hyper-/ultra-compact H II regions (e.g., Kurtz et al. 2000), and ionized winds and jets (e.g., Guzmán et al. 2014, 2016).

HMCs contain gas and dust near or around sites of recent star formation (Cesaroni 2005). They are characterized by small sizes (≤ 0.1 pc), high gas densities ($n_{\text{H}_2} \geq 10^7 \text{ cm}^{-3}$), and high temperatures ($T_k \geq 100$ K) (Garay & Lizano 1999; Kurtz et al. 2000). Unlike H II regions, these objects present weak or undetectable free–free emission. The lack of free–free emission has been interpreted as being due to an intense mass accretion phase that quenches the development of an H II region (Walmsley et al. 1995; Keto 2002, 2003). Therefore, HMCs are likely the precursors of H II regions. The hot core phase is thought to last about 10^5 years (van Dishoeck & Blake 1998) to 10^6 years (Garrod & Herbst 2006) and represents the most chemically rich phase of the interstellar medium, characterized by the presence of complex organic

molecules such as CH₃OH, CH₃CN, HCOOCH₃, CH₃OCH₃, and CH₃CH₂CN (e.g., Beuther et al. 2005, 2006). The observation of HMCs is important for understanding the evolutionary sequence and physical conditions of massive star formation. Due to the compact and dense nature of HMCs, high angular resolution observations using molecular lines with high critical densities and excitation temperatures are crucial to uncovering their physical conditions and to searching for accretion disks. In recent years, the search for accretion disks in HMCs has been very fruitful, as summarized in the review by Beltrán & de Wit (2016), and Keplerian disk candidates have been found (e.g., Johnston et al. 2015; Chen et al. 2016; Ilee et al. 2016; Beuther et al. 2017).

IRAS 18566+0408 is a high-mass star-forming region located at a kinematic distance of 6.7 kpc (Sridharan et al. 2002), with a total far-infrared luminosity of $\sim 8 \times 10^4 L_{\odot}$ (Zhang et al. 2007) that comes from a single compact ($< 5''$) dust continuum source, indicating the presence of an embedded O8 ZAMS high-mass star (Sridharan et al. 2002). Weak radio continuum emission was detected at 3.6 cm (flux density of 0.7 mJy; Carral et al. 1999) and at 2 cm (flux density of 0.7 mJy; Araya et al. 2005b), suggesting that this source is in a phase prior to the development of a bright ultra-compact H II region. Very recent observations with the VLA in the 6 and 1.3 cm wavelength bands resolved the radio continuum source in four components, consistent with an ionized jet (Hofner et al. 2017). Dense gas traced by CS and CH₃CN, as well as (sub)mm continuum emission, has been observed (Bronfman et al. 1996; Beuther et al. 2002a; Sridharan et al. 2002; Williams et al. 2004). NH₃(1,1) and (2,2) emission were

detected first using single-dish telescopes by Miralles et al. (1994), Molinari et al. (1996), and Sridharan et al. (2002), and later imaged using the VLA (Zhang et al. 2007).

Current star formation in the region is also evident from the presence of 22 GHz H₂O, 6.7 GHz CH₃OH, 8 GHz H₂CO, and 6.03 GHz OH maser emission (Miralles et al. 1994; Slysh et al. 1999; Beuther et al. 2002a, 2002b, 2002c; Araya et al. 2007; Al-Marzouk et al. 2012), as well as the presence of molecular outflows detected in SiO and NH₃ (Zhang et al. 2007) at PA = 135°. Araya et al. (2007) suggest the presence of an ionized jet, inferred by emission at 4.5 μm from *Spitzer* and 3.6 cm continuum from VLA, roughly in the direction of the molecular outflow. This jet has been recently confirmed by Hofner et al. (2017) at ~0''3 angular resolution. Compact and narrow NH₃(3,3) line emission features are found to be associated with the outflow (Zhang et al. 2007), likely arising from weak population inversion similar to maser emission (Zhang & Ho 1995; Zhang et al. 1999). Araya et al. (2007) detected emission at 7 mm of a torus-like structure (PA = 44°) almost perpendicular to the observed ionized jet (PA ~ 100°).

In order to study the physical and kinematical properties of the high-mass star-forming region IRAS 18566+0408, we carried out sub-arcsecond angular resolution observations with the Submillimeter Array (SMA) in both continuum and molecular line emission. IRAS 18566+0408 has a bipolar molecular outflow, which is expected to be associated to a disk. Our main goal is to search for the presence or absence of disk-like structure(s) around the high-mass star(s) driving the molecular outflow. This paper is organized as follows. In Section 2 we summarize the observations, in Section 3 we present the results, and in Section 4 we discuss and conclude the main findings of the investigation.

2. Observations

Observations of IRAS 18566+0408 were carried out with the SMA⁷ (Ho et al. 2004) using two different configurations. Compact-array observations were taken on 2007 July 9 at 2''4 angular resolution. Very-extended configuration data were obtained on 2008 August 3 at 0''4 angular resolution. Two spectral sidebands, 2 GHz wide and separated by 10 GHz, covered the frequency ranges of 219.4–221.3 GHz and 229.3–231.2 GHz. The receivers were tuned to 230.538 GHz in the upper sideband, with a channel spacing of 0.53 km s⁻¹. The primary beam of the SMA at 225 GHz is 56''. The phase reference center of the observation was set to the position α(J2000) = 18^h59^m09^s.99 and δ(J2000) = 04°12'15".7. Quasars J1751+096 and J1830+063 were observed to monitor the time-dependent antenna gains in both configurations. For the compact configuration the flux was scaled by observing the asteroid Vesta. For the very-extended configuration the flux calibration was achieved by observing MWC349 and the Jovian satellite Callisto. For bandpass calibration, quasars 3C 273 and 3C 454.3 were observed for the compact and very-extended configuration, respectively. The data from different configurations were calibrated separately using the IDL-based MIR package. The imaging and data analysis were done with the MIRIAD software package (Sault et al. 1995).

⁷ The SMA is a joint project between the Smithsonian Astrophysical Observatory and the Academia Sinica Institute of Astronomy and Astrophysics, and is funded by the Smithsonian Institution and the Academia Sinica.

The continuum emission was produced by averaging the line-free channels in the visibility domain. The 1σ noises for the continuum emission were 3.7 and 1.1 mJy beam⁻¹ for the compact and very-extended configurations, respectively. For spectral lines, the 1σ noises were 55 and 45 mJy beam⁻¹ per channel for the compact and very-extended configurations, respectively (see Table 1 for detected lines).

Since the extent of the shortest baseline in the SMA observations is 12 m, corresponding to ~30'' at 225 GHz, more extended spatial structures are resolved out. This spatial filtering mainly affects the low density tracers, such as ¹²CO(2–1) at velocities close to the systemic velocity of the cloud (v_{lsr} = 85.2 km s⁻¹).

To recover the missing short spacing information, we observed the ¹²CO(2–1) emission at ~11'' with the IRAM 30 m telescope located in Pico Veleta, Spain. A 140'' × 140'' region centered at the same position of the interferometric observations was observed. The receiver was tuned to 230.538 GHz. The spectra have 0.4 km s⁻¹ spectral resolution and were processed using CLASS. The combination of the SMA and the IRAM data was performed using MIRIAD (Zhang et al. 2000).

3. Results

3.1. Continuum Emission

Figure 1 shows the dust continuum emission at 1.3 mm (225 GHz) obtained with the compact configuration, as well as the observations with the very-extended configuration. The compact configuration shows a bright source elongated along the northeast, southwest direction, similar to the torus structure observed by Araya et al. (2007) at 7 mm, and a weaker component nearly perpendicular that has the same direction of the molecular outflow (see Section 3.5). The integrated emission in the whole region above the 3σ level is 503 mJy. To obtain the flux associated with the more compact emission, we fitted a 2D Gaussian using the CASA software package. The measured integrated intensity was 380 mJy, with a deconvolved size of 2''2 × 1''7 (14,700 × 11,400 au at 6.7 kpc).

For the very-extended configuration the integrated intensity above 3σ is 168 mJy. A 2D Gaussian fit to the most compact emission gives a deconvolved size of 0''8 × 0''5 (5400 × 3300 au at 6.7 kpc) and an integrated intensity of 125 mJy. The dust continuum peak is located at the same position of the 87 and 46 GHz continuum emission peaks detected by Zhang et al. (2007). We detect no emission toward the secondary 87 GHz peak detected by Zhang et al. (2007) at (R.A., decl.)_{J2000} = (18^h59^m09^s.21, 04°12'22".6).

3.2. Spectral Lines

Figure 2 shows the observed spectral bandpass (averaged in time and baseline) of the visibility data set around 220 and 230 GHz of the lower and upper sidebands obtained with the compact configuration. All the lines identified in the very-extended configurations were also detected in the compact configuration (see Table 1 for details).

The spectra reveal a chemically rich core with 31 lines from 14 species with a broad range of energy levels (11.0 K for ¹³CO(2–1), up to 525.6 K for CH₃CN(12₈–11₈)). The identification of lines is based on frequencies and line strengths listed in the Splatalogue Spectral line database.⁸ The lines detected

⁸ <http://www.splatalogue.net/>

Table 1
Parameters of the Observed Lines

Line	Freq. (GHz)	E_u/k_B (K)	Config.	S_{ul}	$1\sigma^a$ ($\frac{\text{mJy km}}{\text{beam s}}$)
CH ₃ CH ₂ CN(24 _{2,22} –23 _{2,21})	219.505	135.6	COM	23.83	0.21
C ¹⁸ O(2–1)	219.560	15.8	COM	2.00	1.19
HNCO(10 _{2,8} –9 _{2,7})	219.737	231.1	COM+VEX	9.60	0.16
HNCO(10 _{0,10} –9 _{0,9})	219.798	58.0	COM+VEX	9.73	0.20
H ¹³ CO(3 _{1,2} –2 _{1,1})	219.909	32.9	COM	2.67	0.16
SO(6 ₅ –5 ₄)	219.949	35.0	COM+VEX	5.95	0.32
CH ₃ OH(8 _{0,8} –7 _{1,6})E	220.079	96.6	COM+VEX	1.21	0.19
H ₂ CCO(11 _{1,11} –10 _{1,10})	220.177	76.4	COM	10.91	0.15
¹³ CO(2–1)	220.399	11.0	COM+VEX	2.00	0.91
CH ₃ CN(12 ₈ –11 ₈)	220.476	525.6	COM+VEX	6.67	0.10
CH ₃ CN(12 ₇ –11 ₇)	220.539	418.6	COM+VEX	7.92	0.10
HNCO(10 _{1,9} –9 _{1,8})	220.585	101.5	COM+VEX	9.52	0.18
CH ₃ CN(12 ₆ –11 ₆)	220.594	325.9	COM+VEX	9.00	0.13
CH ₃ CN(12 ₅ –11 ₅)	220.641	247.4	COM+VEX	9.92	0.12
CH ₃ CH ₂ CN(25 _{2,24} –24 _{2,23})	220.661	143.0	COM	24.80	0.23
CH ₃ CN(12 ₄ –11 ₄)	220.679	183.1	COM+VEX	10.67	0.28
CH ₃ CN(12 ₃ –11 ₃)	220.709	133.2	COM+VEX	11.25	0.22
CH ₃ CN(12 ₂ –11 ₂)	220.730	97.4	COM+VEX	11.6	0.20
CH ₃ CN(12 ₁ –11 ₁)	220.743	76.0	COM+VEX	11.92	0.10
CH ₃ CN(12 ₀ –11 ₀)	220.747	68.9	COM+VEX	12.00	0.11
CH ₃ OH(15 _{4,11} –16 _{3,13})E	229.589	374.4	COM+VEX	1.61	0.19
CH ₃ OH(8 _{–1,8} –7 _{0,7})E	229.759	89.1	COM+VEX	1.77	0.17
CH ₃ OH(19 _{5,15} –20 _{4,16})A ⁺	229.864	578.6	COM	2.00	0.11
CH ₃ OH(3 _{–2,2} –4 _{–1,4})E	230.027	39.8	COM+VEX	0.26	0.19
CH ₃ OCH ₃ (17 _{2,15} –16 _{3,14})	230.234	147.7	COM	2.98	0.19
O ¹³ CS(19–18)	230.317	110.5	COM	19.00	0.11
¹² CO(2–1)	230.538	16.6	COM+VEX	2.00	2.38
OCS(19–18)	231.061	110.9	COM+VEX	19.00	0.22
¹³ CS(5 ₀ –4 ₀)	231.221	26.7	COM+VEX	10.00	0.25
CH ₃ OH(10 _{2,9} –9 _{3,6})A [–]	231.281	165.3	COM+VEX	0.93	0.25
CH ₃ CH ₂ CN(27 _{0,27} –26 _{1,26})	231.312	157.7	COM+VEX	23.17	0.12

Note. The parameters are: molecular line, rest frequency, energy in the upper state, SMA configuration in which the line was detected, line strength, and the sigma for the integrated intensity maps.

^a The noise level per channel is of the order of 50 mJy beam^{–1}. Panels in Figures 3 and 4 have different integration ranges in velocity. In this table, we summarize the 1 σ level used in each panel for each molecule.

include three CO isotopologues (¹²CO, ¹³CO, and C¹⁸O), sulfur-bearing species (SO, O¹³CS, OCS, and ¹³CS), and the dense gas tracers CH₃CN and CH₃OH that usually arise from hot cores.

We produce the integrated intensity maps of all the detected lines. For lines identified in both configurations, we make integrated maps combining the two data sets. Most of the species show compact spatial emission coincident with the dust continuum (Figures 3 and 4). However, some of them show elongated emission in the same direction of the continuum bridge (Figure 5). This direction is the same as that of the molecular outflow discussed in Section 3.5. Table 1 lists the molecular and observational parameters of all the detected lines.

3.3. Temperature

We detect nine components of the CH₃CN(12_{*k*}–11_{*k*}) *k*-ladder with *k* = 0–8 (Table 1). CH₃CN is a symmetric top molecule, with a large line strength and dipole moment (3.91 D). The CH₃CN(12_{*k*}–11_{*k*}) level is well-suited for measuring the gas temperature in hot cores (e.g., Pankonin et al. 2001; Araya et al. 2005a; Qiu & Zhang 2009). Since radiative processes across *k*-ladders are forbidden, the population in the different *k*-ladders

can be used to estimate the kinetic temperature even if the levels are not fully thermalized.

We have simultaneously fit all CH₃CN transitions with the simple model described by Araya et al. (2005a) and Zhang et al. (1998), assuming local thermodynamic equilibrium conditions.⁹ The separation of the different transitions is restricted by their rest frequency and we have assumed that all lines have the same velocity dispersion and filling factor. The free parameters in the fitting are the rotational temperature, column density, line width, and filling factor. The optical depth was calculated using the best-fit temperature, column density, and line width, following Equation A8 of Araya et al. (2005a; we detected no isotopologue of CH₃CN).

The CH₃CN spectra and the best-fit model are shown in Figure 6. The best fit resulted in a rotational temperature, T_{rot} , of 240 ± 20 K and a column density, N_{tot} , of $(7.3 \pm 1.0) \times 10^{16}$ cm^{–2}, values similar to those found in other hot cores (Galván-Madrid et al. 2010; Cesaroni et al. 2011; Qiu et al. 2012).

⁹ The Python script used for fitting the CH₃CN(12_{*k*}–11_{*k*}) transitions and determining the rotational temperature and column density can be obtained from the following link: <https://github.com/xinglunju/emanon>.

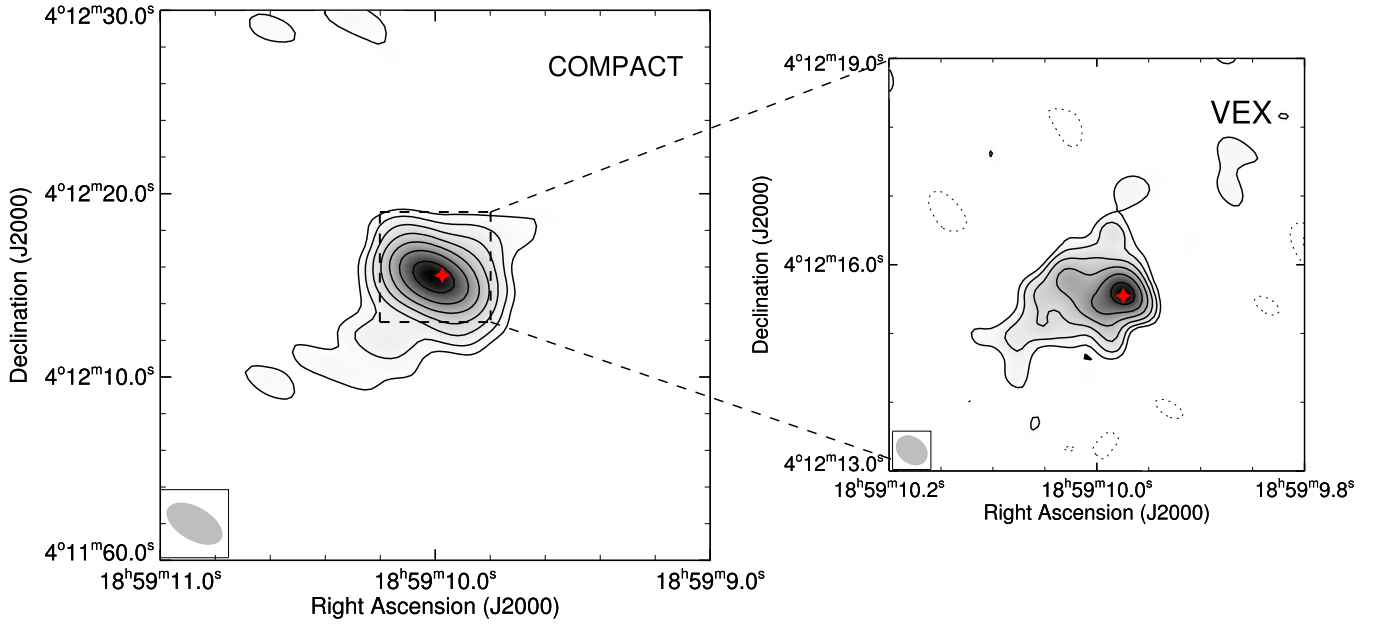


Figure 1. Left: 1.3 mm continuum emission observed with the compact configuration ($\theta = 2''.4$). The contour levels start at 3σ ($1\sigma = 3.71 \text{ mJy beam}^{-1}$) and increase in steps of $\log(\sigma) = 0.2$. Right: continuum emission obtained with the very-extended configuration ($\theta = 0''.4$). The same contour levels are plotted ($1\sigma = 1.1 \text{ mJy beam}^{-1}$). The position of the peak continuum emission detected with the very-extended configuration is indicated with the red star. The synthesized beams are shown in the bottom left corners. Negative features are shown with contours in dashed lines. The peak offset between the two configuration images is less than the smallest beam-size, therefore they are coincident.

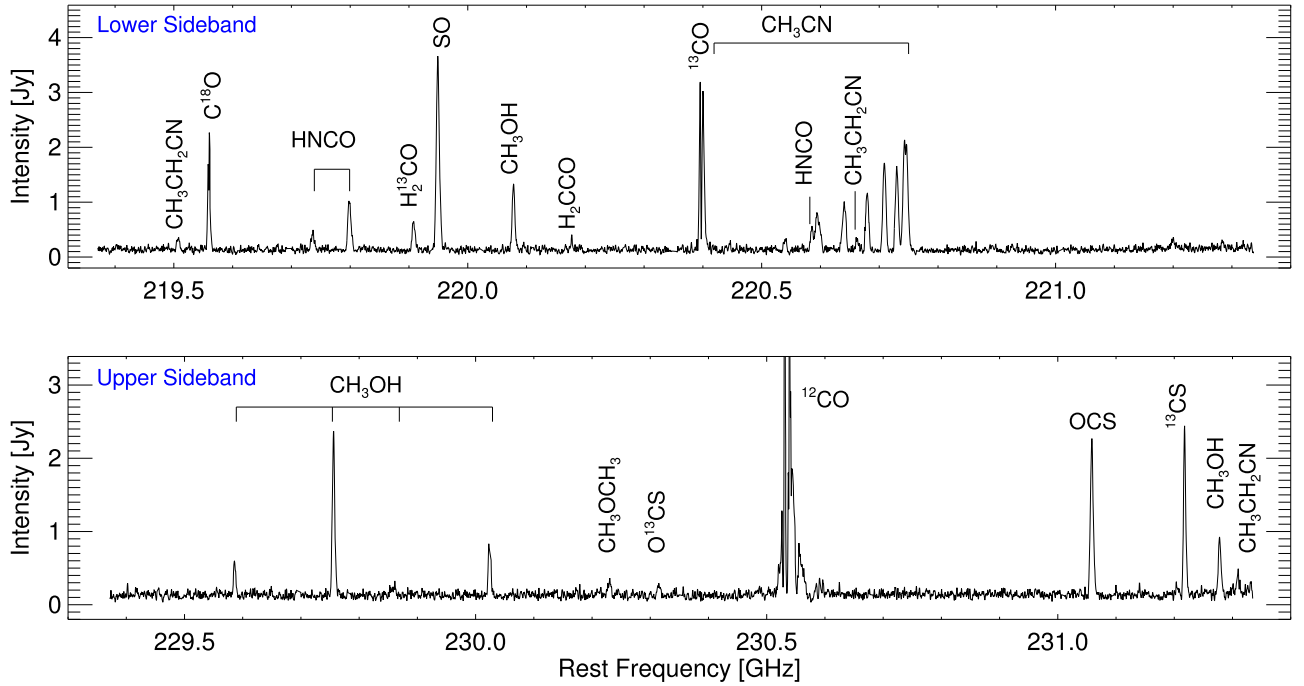


Figure 2. Upper and lower sideband spectra, time-averaged over all baselines for the compact configuration. The spectral resolution is 0.5 km s^{-1} per channel. The identified molecular lines are marked. The peak emission of $^{12}\text{CO}(2-1)$ is 5.2 Jy .

3.4. Mass of the Core

Zhang et al. (2007) derived a spectral index of $\beta = 1.3$ by fitting a graybody to the SED of IRAS 18566+0408, indicating that the entire millimeter continuum from the source is attributable to thermal emission from dust. We adopt the rotational temperature $T = 45 \text{ K}$ derived by Zhang et al. (2007) using NH_3 line observations as the dust temperature in the region, since this is more representative of the extension of the dust emission in the compact configuration. For optically thin

and isothermal emission, the mass of the core can be obtained from the expression

$$M_{\text{gas}} = \frac{S_{1.3 \text{ mm}} D^2}{R_{\text{dg}} k_{1.3 \text{ mm}} B_{1.3 \text{ mm}}(T_{\text{d}})}, \quad (1)$$

where $S_{1.3 \text{ mm}}$ is the integrated flux density at 1.3 mm, D is the distance to the source, R_{dg} is the dust-to-gas mass ratio with a value of 0.01, $B_{1.3 \text{ mm}}(T_{\text{d}})$ is the Planck function at the dust temperature T_{d} , and $k_{1.3 \text{ mm}}$ is the dust absorption coefficient

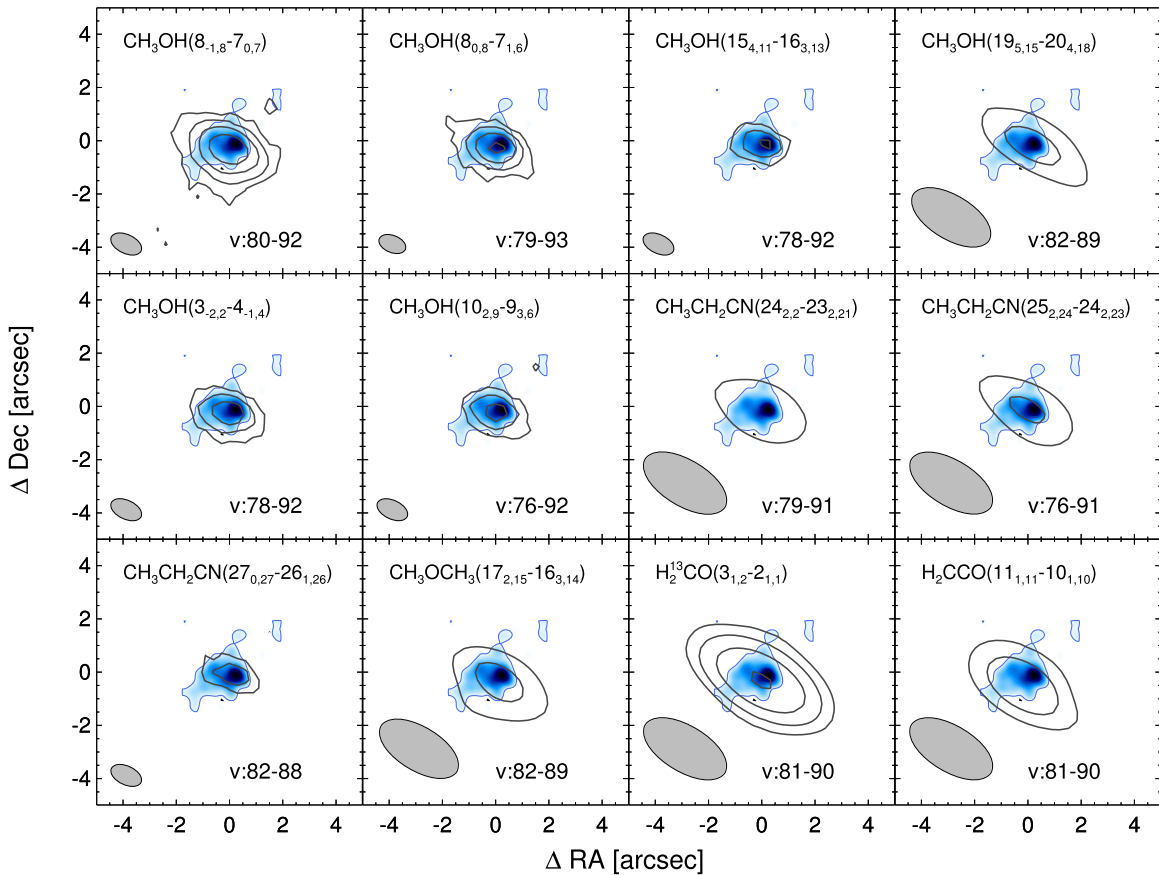


Figure 3. Integrated intensity maps of the detected molecular transitions. The contour levels start at 3σ and are in steps of 6σ (see Table 1 for the σ values). The names of the molecular lines are shown at the top of the images. The synthesized beams and range of integration (in km s^{-1}) are shown at the bottom of each panel. Large beams correspond to images obtained with the compact configuration ($\sim 2''/4$), while smaller beams correspond to those obtained combining the compact + very-extended configurations ($0''/9$). The blue filled contours correspond to the continuum emission obtained with the very-extended configuration.

assumed to be equal to $0.9 \text{ cm}^2 \text{ g}^{-1}$ at 230 GHz (Ossenkopf & Henning 1994).

Assuming $T = 45 \text{ K}$ and using the integrated flux from the 2D Gaussian fitting, we obtain a gas mass of 150 and $50 M_{\odot}$ for the compact and the very-extended configuration, respectively. Using the temperature of 240 K derived from the k -ladders of the $\text{CH}_3\text{CN}(12-11)$ line, the measured mass for the very-extended configuration is $8 M_{\odot}$. This mass of $8 M_{\odot}$ corresponds to the mass of the central, dense compact ($\sim 4000 \text{ au}$) hot core.

3.5. Molecular Outflow

The $^{12}\text{CO}(2-1)$, $^{13}\text{CO}(2-1)$, and $\text{SO}(6_5-5_4)$ spectra show emission in an extended velocity range (Figure 7). The CO isotopologue spectra show dips around the systemic velocity $v_{\text{lsr}} = 85.2 \text{ km s}^{-1}$. The dips are likely caused by both self-absorption and the missing flux of the extended cloud envelope in the interferometer data. The interferometric spatial filtering affects the $^{12}\text{CO}(2-1)$ line strongest since it is the most abundant isotopologue and traces the most extended regions that cannot be covered by the shortest baselines of the interferometer. We recover the missing flux of $^{12}\text{CO}(2-1)$ by combining in the visibility domain the single-dish data from the IRAM 30 m telescope and the interferometric data (Zhang et al. 2000).

Figure 8 shows the channel maps produced using the SMA +IRAM observations of $^{12}\text{CO}(2-1)$. The channel maps show

emission extending in the northwest, southeast direction in a velocity range of $\Delta v = 30 \text{ km s}^{-1}$, tracing a molecular outflow in the same direction as the bipolar molecular outflow delineated in SiO emission by Zhang et al. (2007). Figure 9 shows the integrated intensity maps of the wing emission for the $^{12}\text{CO}(2-1)$, $^{13}\text{CO}(2-1)$, and $\text{SO}(6_5-5_4)$ lines. We excluded in the integration the velocity range associated with the ambient cloud ($81-89 \text{ km s}^{-1}$), as defined by molecular emission that seems unaffected by the outflow.

The outflow maps reveal emission centered at the position of the dust core. Using the $^{12}\text{CO}(2-1)$ line from the combined interferometric and single-dish data set, we compute the mass, momentum, and energy of the outflow following the procedure described in Cabrit & Bertout (1986). We assume optically thin emission and an excitation temperature of 70 K. With a total mass of $16.8 M_{\odot}$, the molecular outflow is consistent with other molecular outflows found in high-mass star-forming regions (e.g., Zhang et al. 2001, 2005; Beuther et al. 2002b). It has a mass $\sim 60\%$ lower than the $27 M_{\odot}$ derived by Zhang et al. (2007) using SiO. This discrepancy can be produced by the more uncertain conversion factor from SiO to an H_2 column than from CO to H_2 , and by the assumption of optically thin CO emission. Indeed, CO wing emission with an optical depth of 1 would increase the mass to the same value measured using SiO. The parameters of the outflow are shown in Table 2.

Zhang et al. (2007) identified four compact and narrow-line $\text{NH}_3(3,3)$ emission features that likely arise from a weak population inversion (labeled as “A,” “B,” “C,” and “D” in

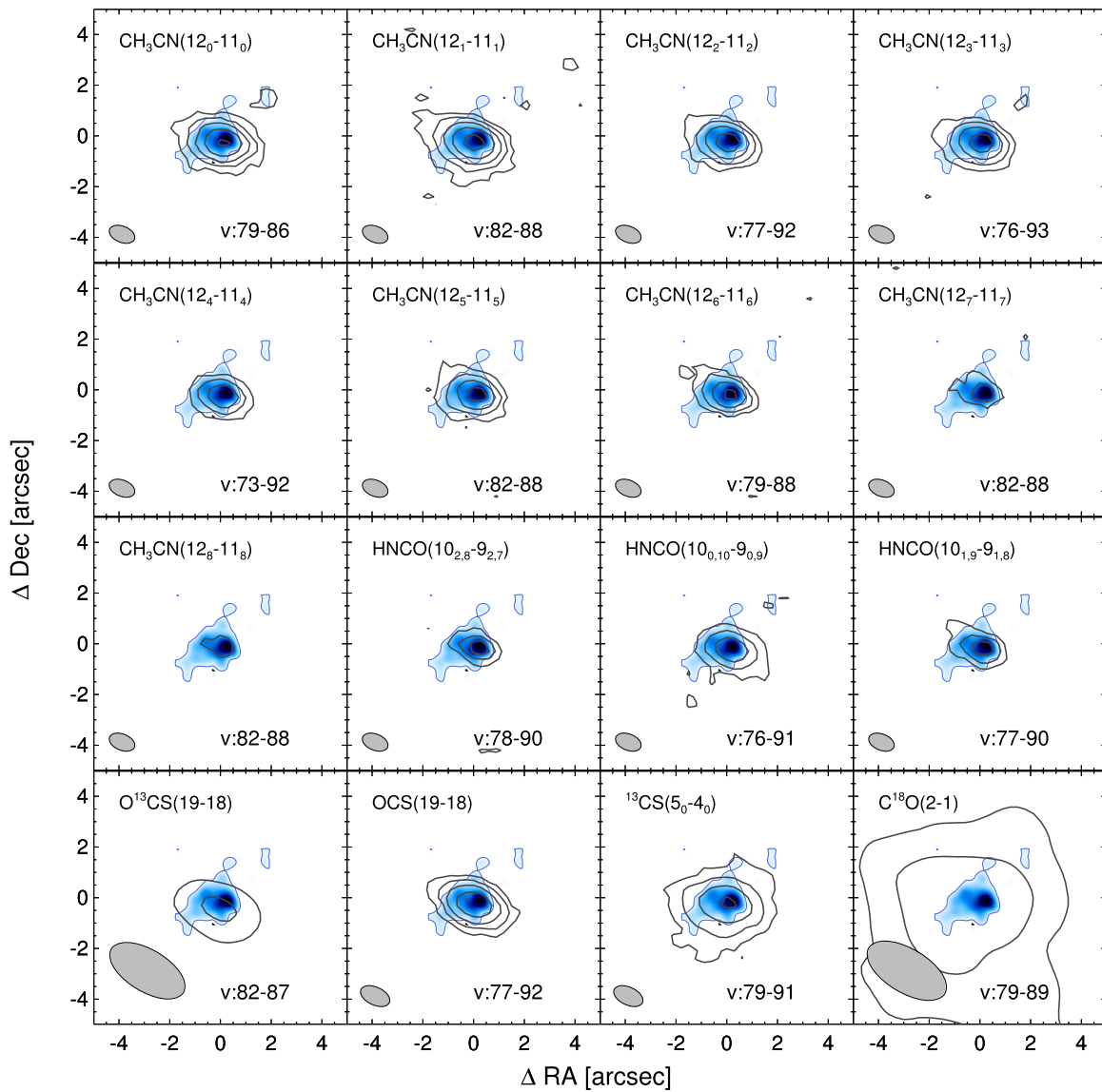


Figure 4. Continuation of Figure 3.

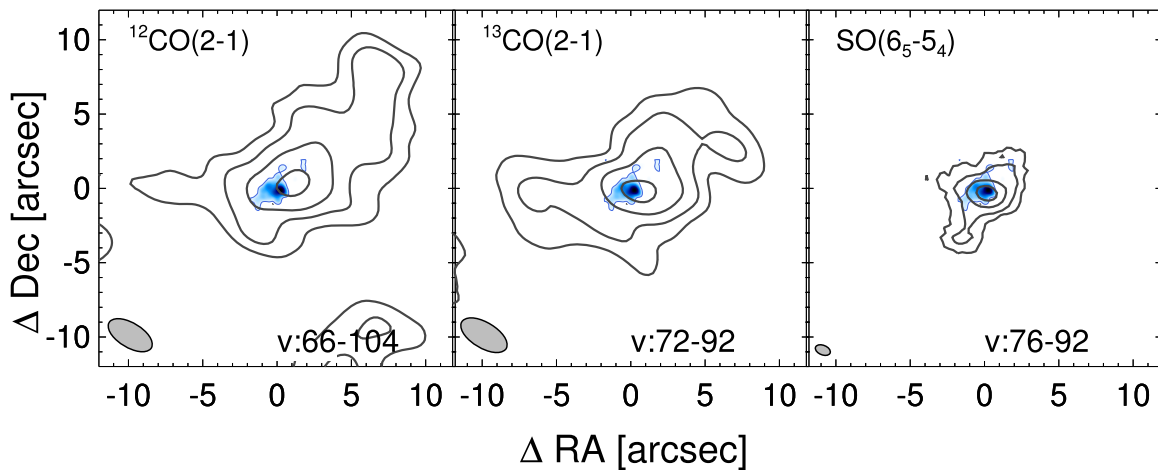


Figure 5. Integrated intensity maps of detected molecular lines with emission at high velocities. The contour levels start at 3σ and are in steps of 3σ (σ values are shown in Table 1). The range of integration (in km s^{-1}) is indicated in the bottom right corners. These maps were created using only SMA data.

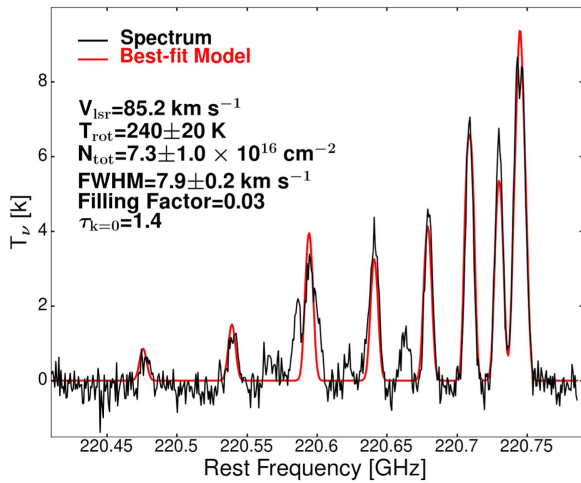


Figure 6. Spectra and best-fit model of the $\text{CH}_3\text{CN}(12_k-11_k)$ $k = 0-8$ lines. The black line shows the observed CH_3CN transitions, while the red line shows the synthetic spectra obtained from the best-fit model. The resultant parameters from the fit (central velocity, rotational temperature, total column density, full width at half maximum, filling factor, and opacity) are indicated.

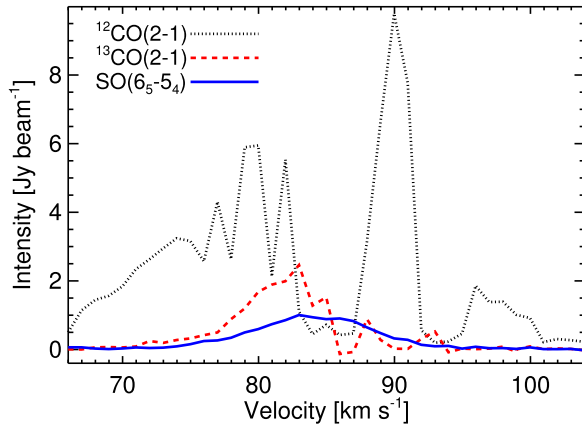


Figure 7. Spectra of the $^{12}\text{CO}(2-1)$, $^{13}\text{CO}(2-1)$, and $\text{SO}(6_5-5_4)$ lines toward the position of the dust peak. The lines have widths up to 50 km s^{-1} .

Figures 8 and 9). They suggest that these $\text{NH}_3(3,3)$ features are associated with the outflow activity in the region and that “C” and “D” could be part of an outflow driven by an undetected core located between them. We detect no dust continuum core (nor hot core line emission) between “C” and “D” and no hint of a molecular outflow other than the one driven by the bright dust continuum core. Given the position of these features in the channel map of CO, we conclude that they are all associated with the outflow emanating from the massive dust core.

3.6. Velocity Gradients

We investigated the velocity gradients for all the detected lines in IRAS 18566+0408 and found no clear trend for rotational structures at 4000 au scales. As an example, we present in Figure 10 the moment-one and the position–velocity maps for three spectral lines ($\text{CH}_3\text{OH}(10_{2,9}-9_{3,6})\text{A}$, $\text{CH}_3\text{CN}(12_3-11_3)$, and $\text{OCS}(19-18)$). Position–velocity maps were made in a direction roughly perpendicular to the direction of the molecular outflow. The absence of velocity gradients does not rule out the existence of an accretion disk (sizes < 1000 au) feeding the central high-mass star(s), but discards

the presence of a toroidal-rotating structure at several-thousand-au scales.

4. Discussion and Conclusion

We detected a variety of spectral lines as well as 1.3 mm continuum emission that allowed us to measure the mass and temperature of the compact core embedded in IRAS 18566+0408. Molecular emission at high velocities (e.g., CO and SO) reveals a bipolar molecular outflow for which we determine its properties. This molecular outflow is roughly perpendicular to the torus-like structure detected by Araya et al. (2007) at 7 mm continuum emission (also seen at the low angular resolution with SMA). However, molecular tracers often used to study core rotation (e.g., CH_3CN) show no clear signs of rotating structures.

Theories of massive star formation predict that outflows must be powered and fed by accretion disks. Evidence of rotation and infall that hint at the presence of disks has been detected in several systems (e.g., Cesaroni et al. 1997, 2005, 2011; Zhang et al. 1998, 2009; Beuther et al. 2007, 2017; Beltrán et al. 2011; Fallscheer et al. 2011; Qiu et al. 2012; Guzmán et al. 2014; Johnston et al. 2015; Chen et al. 2016; Ilee et al. 2016). However, the velocity structures shown in Figure 10 indicate that there is no dominant angular momentum axis in the hot core at a spatial scale of 4000 au. The size-scale of the accretion disk responsible for driving the CO outflow must be much smaller. Small disks are expected in dense cluster-forming regions, as cores harboring massive stars tend to fragment and form multiple stars. The dynamical interactions limit the size of circumstellar disks. In addition, the complex velocity structures seen in the CH_3OH , CH_3CN , and OCS emission may also be partly due to the influence of the molecular outflow, which affects the kinematics and chemistry of the gas.

High-mass stars are overwhelmingly observed in binary or multiple systems. Indeed, in a high-resolution spectroscopic survey including nearly 800 O- and B-type stars, 82% of high-mass stars were found in close binary systems (Chini et al. 2012). In addition, the majority of high-mass stars are paired with high-mass companions (Kobulnicky & Fryer 2007; Chini et al. 2012). We cannot rule out the formation of a binary or multiple system embedded in the IRAS 18566+0408 hot core. By comparing the structure of the continuum emission observed with the compact and very-extended configurations, we can see that some substructures are detected, but not resolved. It is possible that rotational motions are present on smaller scales that are inaccessible with our SMA observations. Indeed, in the nearby high-mass star-forming region NGC 6334I, at least 4 high-mass stars are in the process of formation in less than 2500 au (Brogan et al. 2016). Higher spatial resolution will be needed to search for possible multiplicity in IRAS 18566+0408.

Leurini et al. (2011) and recently Beuther et al. (2017) suggest that in IRAS 17233–3606 the CH_3CN emission, typically used to reveal rotating structures (toroid-disk-like), can be affected by molecular outflows. This is particularly interesting in the study of Beuther et al. (2017) at $0''.06$ resolution (130 au scales), in which the P – V diagrams show Keplerian motions and contamination that is attributed to both infall and molecular outflows even in high-excitation $\text{CH}_3\text{CN}(37_k-36_k)$ transitions ($E_u \sim 1000$ K). Therefore, high angular resolution observations in IRAS 18566+0408 are not only necessary to resolve possible further fragmentation, but

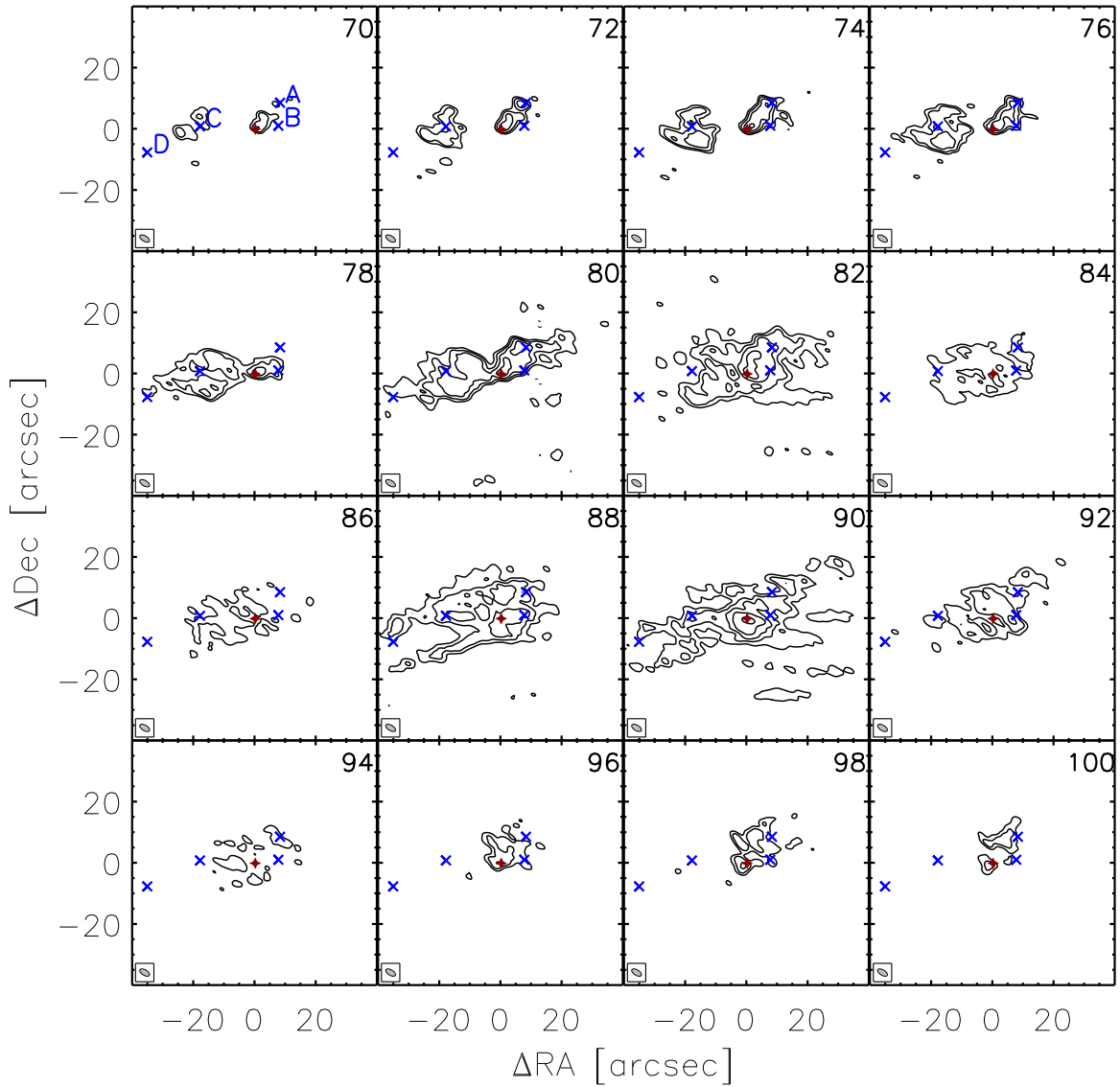


Figure 8. Channel map of the SMA+IRAM observations of the $^{12}\text{CO}(2-1)$ line. The velocities are indicated at the top right corner in km s^{-1} . The beam size is shown at the bottom left corner. The contours start at 9σ and are in steps of 9σ ($1\sigma = 60 \text{ mJy beam}^{-1}$). The $\text{NH}_3(3,3)$ features detected by Zhang et al. (2007) are indicated with the blue crosses, while the dust peak is indicated with the red star.

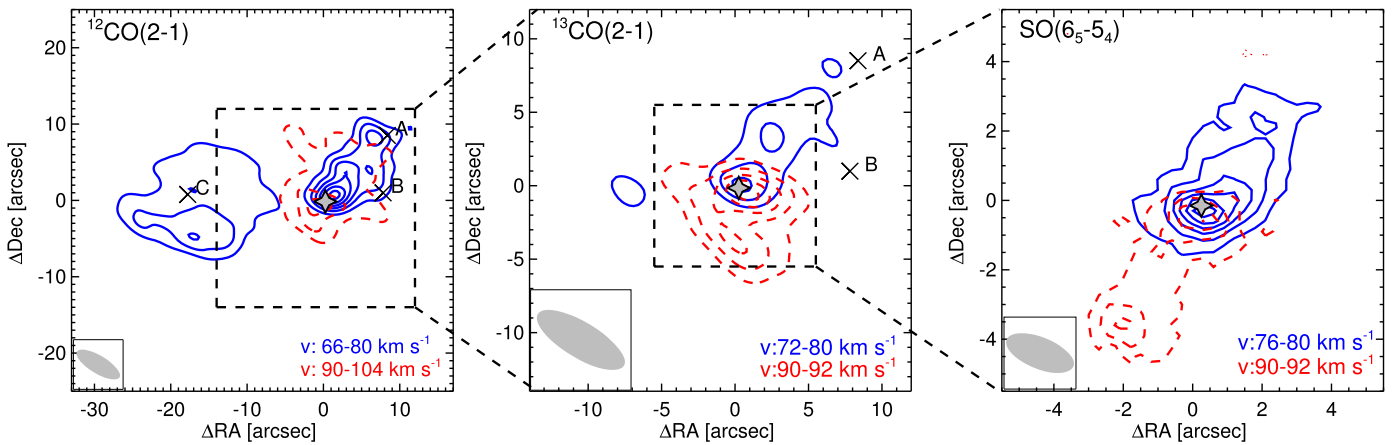


Figure 9. From left to right, blueshifted and redshifted emission obtained for the $^{12}\text{CO}(2-1)$, $^{13}\text{CO}(2-1)$, and $\text{SO}(6_5-5_4)$ lines, respectively. The dashed boxes indicate the region for more compact emission shown at the right side. The contour levels start at 9σ , 6σ , and 3σ and are in steps of 9σ , 6σ , and 3σ for $^{12}\text{CO}(2-1)$, $^{13}\text{CO}(2-1)$, and $\text{SO}(6_5-5_4)$, respectively. The range of velocity integration is indicated in the bottom right in each box. The beam sizes are shown in the bottom left corners. The $\text{NH}_3(3,3)$ features detected by Zhang et al. (2007) are indicated with the crosses, while the dust peak is indicated with the gray star.

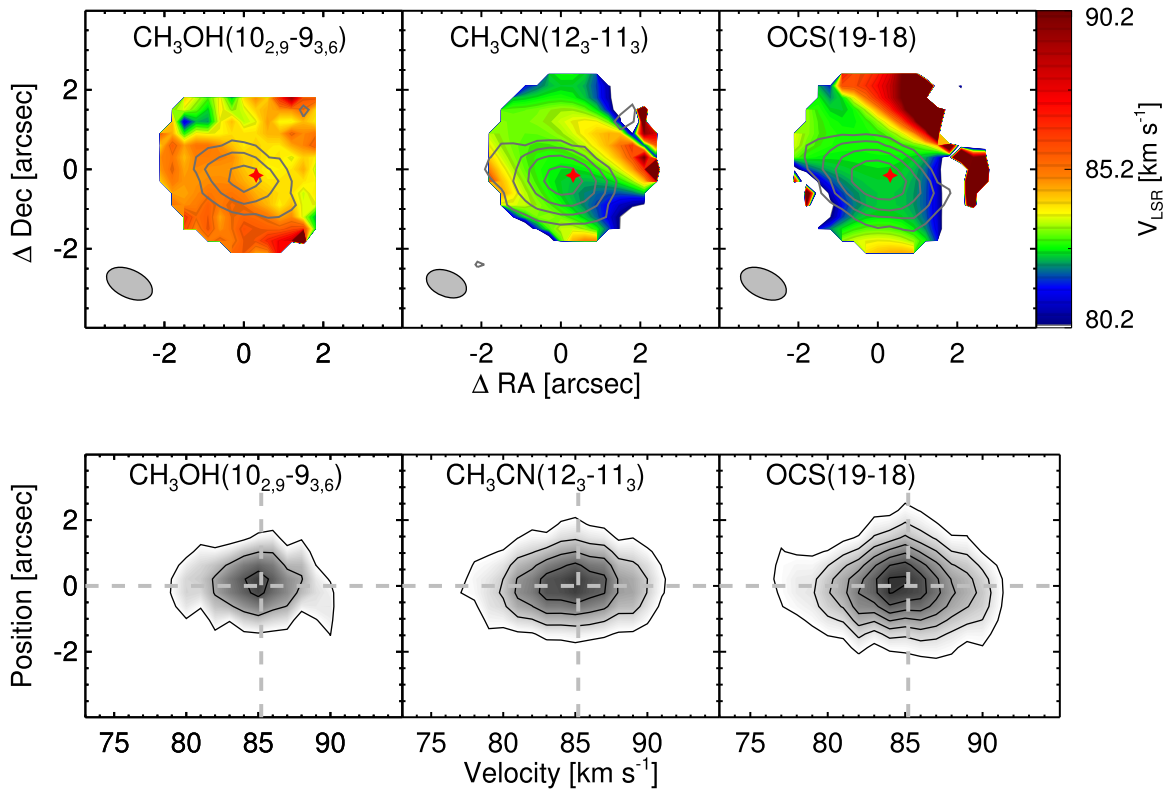


Figure 10. Top: moment-one maps (color scale) for some of the lines with the highest energy levels (Table 1) overplotted with the moment-zero maps (gray lines). Bottom: the position–velocity maps for the respective lines. We find no clear trend for rotational structures.

Table 2
Parameters of the Outflow Derived from the $^{12}\text{CO}(2-1)$ Emission

Lobe	Mass (M_{\odot})	Momentum ($M_{\odot} \text{ km s}^{-1}$)	Energy ($M_{\odot} \text{ km}^2 \text{ s}^{-2}$)
Blue	11.4	105	600
Red	5.4	45	240
Total	16.8	150	840

also to clarify if CH_3CN and the other observed hot core tracers have contamination from processes other than rotation that are unresolved at the SMA angular resolution, precluding the detection of disks. Interestingly, the recent observations of $\text{CH}_3\text{CN}(5-4)$ in IRAS 18566+0408 at $1''$ resolution by Hofner et al. (2017) show a velocity gradient in the direction of the jet/outflow. Their observations support the idea that CH_3CN emission can be contaminated by outflowing gas. This velocity gradient is likely not evident in our $\text{CH}_3\text{CN}(12-11)$ lines because the higher transitions will be excited at higher temperatures, closer to the high-mass star and confusion from both physical processes, rotation, and outflowing gas can be more important than they are at lower-energy transitions. This is supported by the lower filling factor of 0.03 derived in this work for $\text{CH}_3\text{CN}(12-11)$ with respect to the 0.17 derived by Hofner et al. (2017) for $\text{CH}_3\text{CN}(5-4)$.

In summary, we have examined the continuum and spectral line emission and draw the following conclusions:

1. Using SMA in the compact and very-extended configurations, we have observed 1.3 mm continuum and molecular line emission toward IRAS 18566+0408 to reveal a chemically rich, compact core with a mass of $8 M_{\odot}$ ($50 M_{\odot}$ at 45 K) and

central temperature of 240 K that drives a bipolar molecular outflow with a total mass of $16.8 M_{\odot}$.

2. The molecular outflow in CO and SO is consistent with the previously detected outflow in SiO. The molecular outflow is roughly perpendicular to the torus structure detected in continuum emission with the compact configuration (also detected by Araya et al. 2007). However, this torus shows substructures at higher angular resolution and presents no velocity gradients that would suggest a toroidal-disk-like rotating structure.

3. We suggest that the lack of rotational structures is due to the multiplicity of high-mass stars embedded in the hot core and possibly the influence of the outflow (and maybe infall) in the hot core tracers used to search for velocity gradients. Higher angular resolution, likely with ALMA, can confirm or refute both scenarios.

We thank the anonymous referee for helpful comments that improved the paper. Data analysis was in part carried out on the open use data analysis computer system at the Astronomy Data Center, ADC, of the National Astronomical Observatory of Japan.

Facilities: SMA, IRAM.

Software: MIRIAD (Sault et al. 1995), Python,¹⁰ emanon,¹¹ CASA (McMullin et al. 2007), CLASS.¹²

ORCID iDs

Andrea Silva <https://orcid.org/0000-0001-9500-604X>

Qizhou Zhang <https://orcid.org/0000-0003-2384-6589>

Patricio Sanhueza <https://orcid.org/0000-0002-7125-7685>

¹⁰ <https://www.python.org>

¹¹ <https://github.com/xinglunju/emanon>

¹² <http://www.iram.fr/IRAMFR/GILDAS>

Xing Lu  <https://orcid.org/0000-0003-2619-9305>
 Maria T. Beltran  <https://orcid.org/0000-0003-3315-5626>
 Henrik Beuther  <https://orcid.org/0000-0002-1700-090X>
 Riccardo Cesaroni  <https://orcid.org/0000-0002-2430-5103>

References

- Al-Marzouk, A. A., Araya, E. D., Hofner, P., et al. 2012, *ApJ*, **750**, 170
 Araya, E., Hofner, P., Kurtz, S., Bronfman, L., & DeDeo, S. 2005a, *ApJS*, **157**, 279
 Araya, E., Hofner, P., Kurtz, S., et al. 2005b, *ApJ*, **618**, 339
 Araya, E., Hofner, P., Sewilo, M., et al. 2007, *ApJ*, **669**, 1050
 Beltrán, M. T., Cesaroni, R., Zhang, Q., et al. 2011, *A&A*, **532**, A91
 Beltrán, M. T., & de Wit, W. J. 2016, *A&ARv*, **24**, 6
 Beuther, H., Schilke, P., Menten, K. M., et al. 2002a, *ApJ*, **566**, 945
 Beuther, H., Schilke, P., Sridharan, T. K., et al. 2002b, *A&A*, **383**, 892
 Beuther, H., Walsh, A., Schilke, P., et al. 2002c, *A&A*, **390**, 289
 Beuther, H., Walsh, A. J., Johnston, K. G., et al. 2017, arXiv:1703.07235
 Beuther, H., Zhang, Q., Bergin, E. A., et al. 2007, *A&A*, **468**, 1045
 Beuther, H., Zhang, Q., Greenhill, L. J., et al. 2005, *ApJ*, **632**, 355
 Beuther, H., Zhang, Q., Reid, M. J., et al. 2006, *ApJ*, **636**, 323
 Brogan, C. L., Hunter, T. R., Cyganowski, C. J., et al. 2016, *ApJ*, **832**, 187
 Bronfman, L., Nyman, L.-A., & May, J. 1996, *A&AS*, **115**, 81
 Cabrit, S., & Bertout, C. 1986, *ApJ*, **307**, 313
 Carral, P., Kurtz, S., Rodríguez, L. F., et al. 1999, *RMxAA*, **35**, 97
 Cesaroni, R., Beltrán, M. T., Zhang, Q., Beuther, H., & Fallscheer, C. 2011, *A&A*, **533**, A73
 Cesaroni, R., Felli, M., Testi, L., Walmsley, C. M., & Olmi, L. 1997, *A&A*, **325**, 725
 Cesaroni, R. 2005, in *IAU Symp. 227, Massive Star Birth: A Crossroads of Astrophysics*, ed. R. Cesaroni, M. Felli, E. Churchwell, & M. Walmsley (Cambridge: Cambridge Univ. Press), 59
 Cesaroni, R., Neri, R., Olmi, L., et al. 2005, *A&A*, **434**, 1039
 Chen, H.-R. V., Keto, E., Zhang, Q., et al. 2016, *ApJ*, **823**, 125
 Chini, R., Hoffmeister, V. H., Nasserri, A., Stahl, O., & Zinnecker, H. 2012, *MNRAS*, **424**, 1925
 Cyganowski, C. J., Brogan, C. L., Hunter, T. R., et al. 2012, in *IAU Symp. 287, Cosmic Masers—from OH to H0*, ed. R. S. Booth, W. H. T. Vlemmings, & E. M. L. Humphreys (Cambridge: Cambridge Univ. Press), 127
 Fallscheer, C., Beuther, H., Sauter, J., Wolf, S., & Zhang, Q. 2011, *ApJ*, **729**, 66
 Galván-Madrid, R., Zhang, Q., Keto, E., et al. 2010, *ApJ*, **725**, 17
 Garay, G., & Lizano, S. 1999, *PASP*, **111**, 1049
 Garrod, R. T., & Herbst, E. 2006, *A&A*, **457**, 927
 Guzmán, A. E., Garay, G., Rodríguez, L. F., et al. 2014, *ApJ*, **796**, 117
 Guzmán, A. E., Garay, G., Rodríguez, L. F., et al. 2016, *ApJ*, **826**, 208
 Ho, P. T. P., Moran, J. M., & Lo, K. Y. 2004, *ApJL*, **616**, L1
 Hofner, P., Cesaroni, R., Kurtz, S., et al. 2017, arXiv:1705.07203
 Ilee, J. D., Cyganowski, C. J., Nazari, P., et al. 2016, *MNRAS*, **462**, 4386
 Johnston, K. G., Robitaille, T. P., Beuther, H., et al. 2015, *ApJL*, **813**, L19
 Keto, E. 2002, *ApJ*, **580**, 980
 Keto, E. 2003, *ApJ*, **599**, 1196
 Kobulnicky, H. A., & Fryer, C. L. 2007, *ApJ*, **670**, 747
 Kurtz, S., Cesaroni, R., Churchwell, E., Hofner, P., & Walmsley, C. M. 2000, in *Protostars and Planets IV*, ed. V. Mannings, A. P. Boss, & S. S. Russell (Tucson, AZ: Univ. Arizona Press), 299
 Leurini, S., Codella, C., Zapata, L., et al. 2011, *A&A*, **530**, A12
 McMullin, J. P., Waters, B., Schiebel, D., Young, W., & Golap, K. 2007, in *ASP Conf. Ser. 376, Astronomical Data Analysis Software and Systems XVI*, ed. R. A. Shaw, F. Hill, & D. J. Bell (San Francisco, CA: ASP), 127
 Miralles, M. P., Rodríguez, L. F., & Scalise, E. 1994, *ApJS*, **92**, 173
 Molinari, S., Brand, J., Cesaroni, R., & Palla, F. 1996, *A&A*, **308**, 573
 Ossenkopf, V., & Henning, T. 1994, *A&A*, **291**, 943
 Pankonin, V., Churchwell, E., Watson, C., & Bieging, J. H. 2001, *ApJ*, **558**, 194
 Qiu, K., & Zhang, Q. 2009, *ApJL*, **702**, L66
 Qiu, K., Zhang, Q., Beuther, H., & Fallscheer, C. 2012, *ApJ*, **756**, 170
 Qiu, K., Zhang, Q., Megeath, S. T., et al. 2008, *ApJ*, **685**, 1005
 Sanchez-Monge, A., Schilke, P., Schmiedeke, A., et al. 2017, arXiv:1704.01805
 Sanhueza, P., Jackson, J. M., Foster, J. B., et al. 2012, *ApJ*, **756**, 60
 Sault, R. J., Teuben, P. J., & Wright, M. C. H. 1995, in *ASP Conf. Ser. 77, Astronomical Data Analysis Software and Systems IV*, ed. R. A. Shaw, H. E. Payne, & J. J. E. Hayes (San Francisco, CA: ASP), 433
 Slysh, V. I., Val'ts, I. E., Kalenskii, S. V., et al. 1999, *A&AS*, **134**, 115
 Sridharan, T. K., Beuther, H., Schilke, P., Menten, K. M., & Wyrowski, F. 2002, *ApJ*, **566**, 931
 van Dishoeck, E. F., & Blake, G. A. 1998, *ARA&A*, **36**, 317
 Walmsley, C. M., Cesaroni, R., Olmi, L., Churchwell, E., & Hofner, P. 1995, *Ap&SS*, **224**, 173
 Wang, K., Zhang, Q., Testi, L., et al. 2014, *MNRAS*, **439**, 3275
 Wang, Y., Zhang, Q., Rathborne, J. M., Jackson, J., & Wu, Y. 2006, *ApJL*, **651**, L125
 Williams, S. J., Fuller, G. A., & Sridharan, T. K. 2004, *A&A*, **417**, 115
 Zhang, Q., & Ho, P. T. P. 1995, *ApJL*, **450**, L63
 Zhang, Q., Ho, P. T. P., & Ohashi, N. 1998, *ApJ*, **494**, 636
 Zhang, Q., Ho, P. T. P., & Wright, M. C. H. 2000, *AJ*, **119**, 1345
 Zhang, Q., Hunter, T. R., Brand, J., et al. 2001, *ApJL*, **552**, L167
 Zhang, Q., Hunter, T. R., Brand, J., et al. 2005, *ApJ*, **625**, 864
 Zhang, Q., Hunter, T. R., Sridharan, T. K., & Cesaroni, R. 1999, *ApJL*, **527**, L117
 Zhang, Q., Sridharan, T. K., Hunter, T. R., et al. 2007, *A&A*, **470**, 269
 Zhang, Q., Wang, Y., Pillai, T., & Rathborne, J. 2009, *ApJ*, **696**, 268